Seismic imaging with Wigner distribution functions

Paul Sava[1] and Oleg Poliannikov[2]
[1] *Center for Wave Phenomena, Colorado School of Mines*
[2] *Department of Earth, Atmospheric and Planetary Sciences, Massachusetts Institute of Technology*

ABSTRACT
The fidelity of depth seismic imaging depends on the accuracy of the velocity models used for wavefield reconstruction. Models can be decomposed in two components corresponding to large scale and small scale variations. In practice, the large scale velocity model component can be estimated with high accuracy using repeated migration/tomography cycles, but the small scale component cannot. When the Earth has significant small-scale velocity components, wavefield reconstruction does not completely describe the recorded data and migrated images are perturbed by artifacts.
There are two possible ways to address this problem: improve wavefield reconstruction by estimating more accurate velocity models and image using conventional techniques (e.g. wavefield cross-correlation), or reconstruct wavefields with conventional methods using the known background velocity model, but improve the imaging condition to alleviate the artifacts caused by the imprecise reconstruction, which is what we suggest in this paper.
We describe the unknown component of the velocity model as a random function with local spatial correlations. Imaging data perturbed by such random variations is characterized by statistical instability, i.e. various wavefield components image at wrong locations that depend on the actual realization of the random model. Statistical stability can be achieved by pre-processing the reconstructed wavefields prior to the imaging condition. We employ Wigner distribution functions to attenuate the random noise present in the reconstructed wavefields, parametrized as a function of image coordinates. Wavefield filtering using Wigner distribution functions and conventional imaging can be lumped-together into a new form of imaging condition which we call an "interferometric imaging condition" due to its similarity to concepts from recent work on interferometry. The interferometric imaging condition can be formulated both for zero-offset and for multi-offset data, leading to robust and efficient imaging procedures that are effective in attenuating imaging artifacts due to unknown velocity models.

Key words: wave-equation, imaging, Wigner distribution functions

1 INTRODUCTION

Seismic imaging in complex media requires accurate knowledge of the medium velocity. Assuming single scattering (Born approximation), imaging requires propagation of the recorded wavefields from the acquisition surface, followed by the application of an imaging condition highlighting locations where backscattering occurs, i.e. where reflectors are present. Typically, this is achieved with simple image processing techniques, e.g. cross-correlation of wavefields reconstructed from sources and receivers.

The main requirement for good-quality imaging is accurate knowledge of the velocity model. Errors in the model used for imaging lead to inaccurate reconstruction of the seismic wavefields and to distortions of the migrated images. In any realistic seismic field experiment the velocity model is never known exactly. Migration velocity analysis estimates large scale approximations of the model, but some fine scale variations always remain elusive. For example, when geology includes complicated stratigraphic structures or complex salt/carbonate bodies, the rapid velocity variations on the scale of the seismic wavelength and smaller cannot be estimated correctly by kinematic methods. Therefore, even if the broad kinematics of the seismic wavefields are reconstructed cor-

rectly, the extrapolated wavefields also contain phase and amplitude distortions that lead to image artifacts obstructing the image of the geologic structure under consideration. While it is certainly true that even the recovery of a long-wave background may prove to be a challenge in some circumstances, we do not attempt to address that issue in this paper. Instead, we concentrate solely on the problem of dealing with the effect of a small scale random variations not estimated by conventional methods.

There are two ways in which we can approach this problem. The first option is to improve our velocity analysis methods to estimate the small-scale variations in the model. Such techniques take advantage of all information contained in seismic wavefields and are not limited to kinematic information of selected events picked from the data. Examples of techniques in this category are waveform inversion (Tarantola, 1987; Pratt & Worthington, 1990; Pratt, 1990; Sirgue & Pratt, 2004), wave-equation tomography (Woodward, 1992) or wave-equation migration velocity analysis (Sava & Biondi, 2004a,b; Shen *et al.*, 2005). A more accurate velocity model allows for more accurate wavefield reconstruction. Then, wavefields can be used for imaging using conventional procedures, e.g. cross-correlation. The second option is to concentrate on the imaging condition, rather than concentrate on "perfect" wavefield reconstruction. Assuming that the large-scale component of the velocity models is known (e.g. by iterative migration/tomography cycles), we can design imaging conditions that are not sensitive to small inaccuracies of the reconstructed wavefields. Imaging artifacts can be reduced at the imaging condition step, despite the fact that the wavefields incorporate small kinematic errors due to velocity fluctuations.

Of course, the two options are complementary to each other, and both can contribute to imaging accuracy. In this paper, we concentrate on the second approach. For purposes of theoretical analysis, it is convenient to model the small-scale velocity fluctuations as random but spatially correlated variations superimposed on a known velocity. We assume that we know the background model, but that we do not know the random fluctuations. The goal is to design an imaging condition that alleviates artifacts caused by those random fluctuations. Conventional imaging consists of cross-correlations of extrapolated source and receiver wavefields at image locations. Since wavefield extrapolation is performed using an approximation of the true model, the wavefields contain random time delays, or equivalently random phases, which lead to imaging artifacts.

One way of mitigating the effects of the random model on the quality of the resulting image is to use techniques based on acoustic time reversal (Fink, 1999). Under certain assumptions, a signal sent through a random medium, recorded by a receiver array, time reversed and sent back through the same medium, refocuses at the source location in a statistically stable fashion. Statistical stability means that the refocusing properties (i.e. image quality) are independent of the actual realization of the random medium (Papanicolaou *et al.*, 2004; Fouque *et al.*, 2005).

We investigate an alternative way of increasing imaging statistical stability. Instead of imaging the reconstructed wavefields directly, we first apply a transformation based on Wigner distribution functions (Wigner, 1932) to the reconstructed wavefields. We consider a special case of the Wigner distribution function (WDF) which has the property that it attenuates random fluctuations from the wavefields after extrapolation with conventional techniques. The idea for this method is borrowed from image processing where WDFs are used for filtering of random noise. Here, we apply WDFs to the reconstructed wavefields, prior to the imaging condition. This is in contrast to data filtering prior to wavefield reconstruction or to image filtering after the application of an imaging condition.

Our procedure closely resembles conventional imaging procedures where wavefields are extrapolated in the image volume and then cross-correlated in time at every image location. Our method uses WDFs defined in three-dimensional windows around image locations which makes it both robust and efficient. From an implementation and computational cost point of view, our technique is similar to conventional imaging, but its statistical properties are improved. Although conceptually separate, we can lump-together the WDF transformation and conventional imaging into a new form of imaging condition which resembles interferometric techniques (Papanicolaou *et al.*, 2004; Fouque *et al.*, 2005). Therefore, we use the name interferometric imaging condition for our technique to contrast it with the conventional imaging condition.

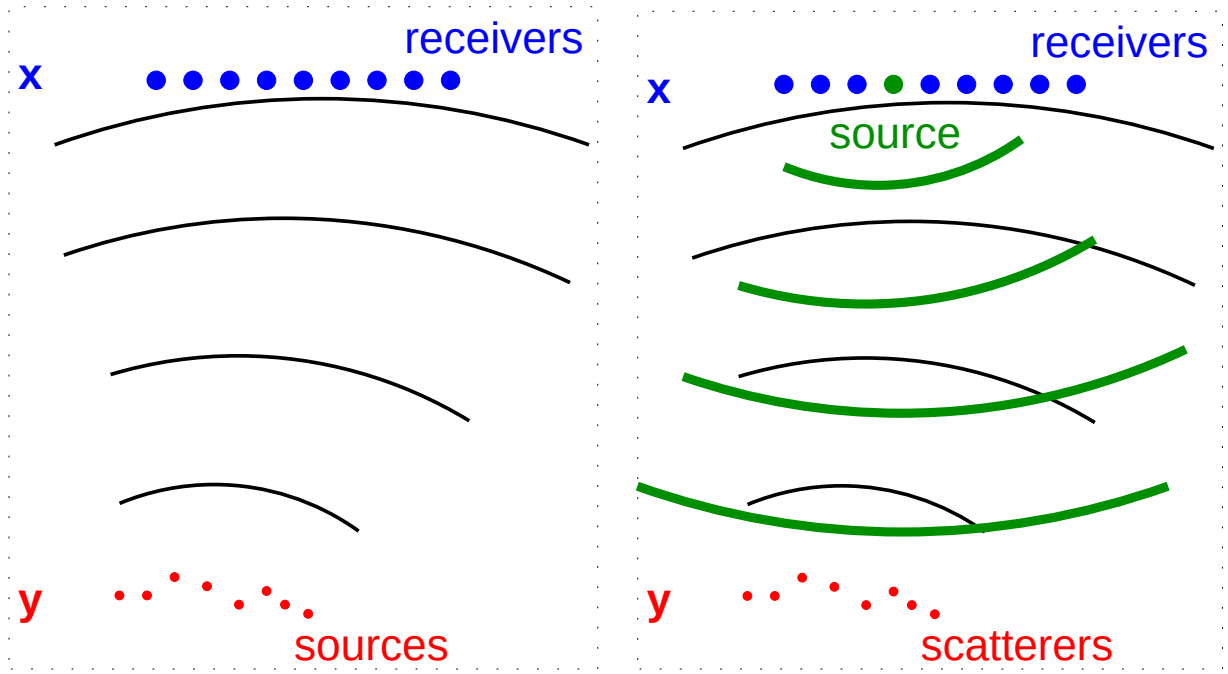
A related method discussed in the literature is known under the name of coherent interferometric imaging (Borcea *et al.*, 2006a,b,c). This method uses similar local cross-correlations and averaging, but unlike our method, it parametrizes reconstructed wavefields as a function of receiver coordinates. Thus, the coherent interferometric imaging functional requires separate wavefield reconstruction from every receiver position, which makes this technique prohibitively expensive and probably unusable in practice on large-scale seismic imaging projects. In contrast, the imaging technique advocated in this paper achieves similar statistical stability properties as coherent interferometric imaging, but at an affordable computational cost since we apply wavefield reconstruction only once for all receiver locations corresponding to a given seismic experiment, typically a "shot".

2 IMAGING CONDITIONS

2. 1 Conventional imaging condition

Let $D(\mathbf{x}, t)$ be the data recorded at time t at receivers located at coordinates $\mathbf{x}$ for a seismic experiment with buried sources (Figure 1(a)) also known as an exploding reflector seismic experiment (Loewenthal *et al.*, 1976). A conventional imaging procedure for this type of data consists of two steps (Claerbout, 1985): wavefield reconstruction at image coordinates $\mathbf{y}$ from data recorded at receiver coordinates $\mathbf{x}$, followed by an imaging condition taking the reconstructed wavefield at time $t = 0$ as the seismic image.

Mathematically, we can represent the wavefield V reconstructed at coordinates $\mathbf{y}$ from data D recorded at coordinates



(a) (b)

Figure 1. Zero-offset seismic experiment sketch (a) and multi-offset seismic experiment sketch (b). Coordinates $\mathbf{x} = \{x, y\}$ characterize receiver positions on the surface and coordinates $\mathbf{y} = \{x, y, z\}$ characterize reflector positions in the subsurface.

$\mathbf{x}$ as a temporal convolution of the recorded trace with the Green's function G connecting the two points:

$$V(\mathbf{x}, \mathbf{y}, t) = D(\mathbf{x}, t) *_t G(\mathbf{x}, \mathbf{y}, t) \ . \tag{1}$$

The total wavefield U reconstructed at $\mathbf{y}$ from all receivers is the superposition of the wavefields V reconstructed from individual traces

$$U(\mathbf{y}, t) = \int_{\mathbf{x}} d\mathbf{x}\, V(\mathbf{x}, \mathbf{y}, t) \ , \tag{2}$$

where the integral over $\mathbf{x}$ spans the entire receiver space. As stated, the imaging condition extracts the image $R(\mathbf{y})$ from the wavefield $U(\mathbf{y}, t)$ at time $t = 0$, i.e.

$$R(\mathbf{y}) = U(\mathbf{y}, t = 0) \ . \tag{3}$$

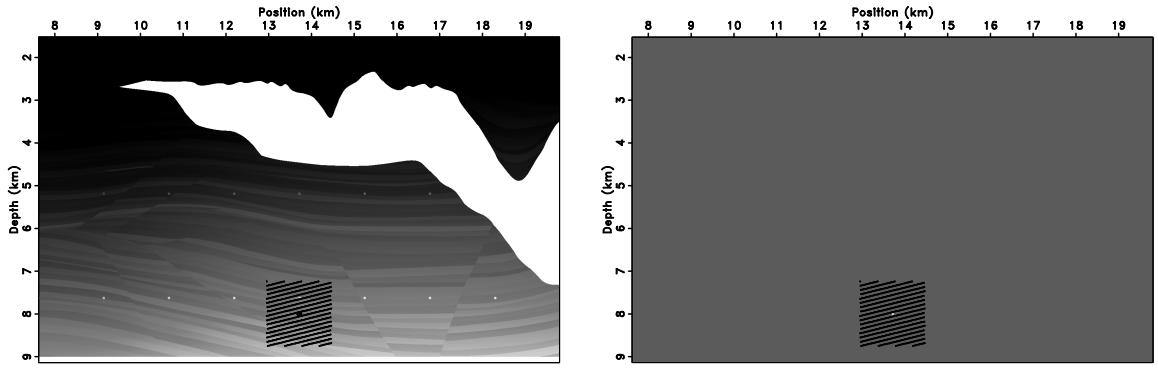
The Green's function used in the procedure described by equation 1 can be implemented in different ways. For our purposes, the actual method used for computing Green's functions is not relevant. Any procedure can be used, although different procedures will be appropriate in different situations, with different cost of implementation. We assume that a satisfactory procedure exists and is appropriate for the respective velocity models used for the simulations. In our examples, we compute Green's functions with time-domain finite-difference solutions to the acoustic wave-equation, similar to reverse-time migration (Baysal *et al.*, 1983).

Consider the velocity model depicted in Figure 2(a) and the imaging target depicted in Figure 2(b). We assume that the model with random fluctuations (Figure 3(b)) represents the real subsurface velocity and use this model to simulate data. We consider the background model (Figure 3(a)) to represent the migration velocity and use this model to migrate the data simulated in the random model. We consider one source located in the subsurface at coordinates $z = 8$ km and $x = 13.5$ km, and receivers located close to the top of the model at discrete horizontal positions and depth $z = 0.0762$ km. Figure 3(c)-3(d) show snapshots of the simulated wavefields at a later time. The panels on the left correspond to modeling in the background model, while the panels on the right correspond to modeling in the random model.

Figure 3(f) shows the data recorded on the surface. The direct wavefield arrival from the seismic source is easily identified in the data, although the wavefronts are distorted by the random perturbations in the medium. For comparison, Figure 3(e) shows data simulated in the background model, which do not show random fluctuations.

Conventional imaging using the procedure described above implicitly states that data generated in the random model, Figure 3(b), are processed as if they were generated in the background model, Figure 3(a). Thus, the random phase variations in the data are not properly compensated during the imaging procedure causing artifacts in the image. Figure 6(b) shows the image obtained by migrating data from Figure 3(f) using the model from Figure 3(a). For comparison, Figure 6(a) shows the image obtained by migrating the data from Figure 3(e) using the same model from Figure 3(a).

Ignoring aperture effects, the artifacts observed in the im-



(a) (b)

Figure 2. Velocity model (a) and imaging target located around $z = 8$ km (b). The shaded area is imaged in Figures 6(a)-6(d).

ages are caused only by the fact that the velocity models used for modeling and migration are not the same. Small artifacts caused by truncation of the data on the acquisition surface can also be observed, but those artifacts are well-known (i.e. truncation butterflies) and are not the subject of our analysis. In this example, the wavefield reconstruction procedure is the same for both modeling and migration (i.e. time-domain finite-difference solution to the acoustic wave-equation), thus it is not causing artifacts in the image. We can conclude that the migration artifacts are simply due to the phase errors between the Green's functions used for modeling (with the random velocity) and the Green's functions used for migration (with the background velocity). The main challenge for imaging in media with random variations is to design procedures that attenuate the random phase delays introduced in the recorded data by the unknown variations of the medium without damaging the real reflections present in the data.

The random phase fluctuations observed in recorded data (Figure 3(f)) are preserved during wavefield reconstruction using the background velocity model. We can observe the randomness in the extrapolated wavefields in two ways, by reconstructing wavefields using individual data traces separately, or by reconstructing wavefields using all data traces at once.

The first option is to reconstruct the seismic wavefield at all image locations $\mathbf{y}$ from *individual* receiver positions on the surface. Of course, this is not conventionally done in reverse-time imaging, but we describe this concept just for illustration purposes. Figure 4(a) shows the wavefield reconstructed separately from individual data traces depicted in Figure 3(f) using the background model depicted in Figure 3(b). In Figure 4(a), the horizontal axis corresponds to receiver positions on the surface, i.e. coordinates $\mathbf{x}$, and the vertical axis represents time. According to the notations used in this paper, Figure 4(a) shows the wavefield $V(\mathbf{x}, \mathbf{y}, t)$ reconstructed to a particular image coordinate $\mathbf{y}$ from separate traces located on the surface at coordinates $\mathbf{x}$. A similar plot can be constructed for all other image locations. Ideally, the reconstructed wavefield should line-up at time $t = 0$, but this is not what we observe in this figure, indicating that the input data contain random phase delays that are not compensated during wavefield reconstruction using the background velocity.

The second option is to reconstruct the seismic wavefield at all image locations $\mathbf{y}$ from *all* receiver positions on the surface at once. This is a conventional procedure for reverse-time imaging. Figure 5(a) shows the wavefield reconstructed from all data traces depicted in Figure 3(f) using the background model depicted in Figure 3(b). In Figure 5(a), the vertical and horizontal axes correspond to depth and horizontal positions around the source, i.e. coordinates $\mathbf{y}$, and the third cube axis represents time. According to the notations used in this paper, Figure 5(a) corresponds to wavefield $U(\mathbf{y}, t)$ reconstructed from data at all receiver coordinates $\mathbf{x}$ to image coordinates $\mathbf{y}$. The reconstructed wavefield does not focus completely at the image coordinate and time $t = 0$ indicating that the input data contains random phase delays that are not compensated during wavefield reconstruction using the background velocity.

2. 2 Wigner distribution functions

One possible way to address the problem of random fluctuations in reconstructed wavefields is to use Wigner distribution functions (Wigner, 1932) to pre-process the wavefields prior to the application of the imaging condition. Appendix C provides a brief introduction for readers unfamiliar with Wigner distribution functions. More details about this topic are presented by Cohen (1995).

Wigner distribution functions (WDF) are bi-linear representations of multi-dimensional signals defined in phase space, i.e. they depend simultaneously on position-wavenumber ($\mathbf{y} - \mathbf{k}$) and time-frequency ($t - \omega$). Wigner (1932) developed these concepts in the context of quantum physics as probability functions for the simultaneous description of coordinates and momenta of a given wave function. WDFs were introduced to signal processing by Ville (1948) and have since found many applications in signal and image processing, speech recognition, optics, etc.

A variation of WDFs, called *pseudo Wigner distribution functions* are constructed using small windows localized in space and/or time (Appendix C). Pseudo WDFs are

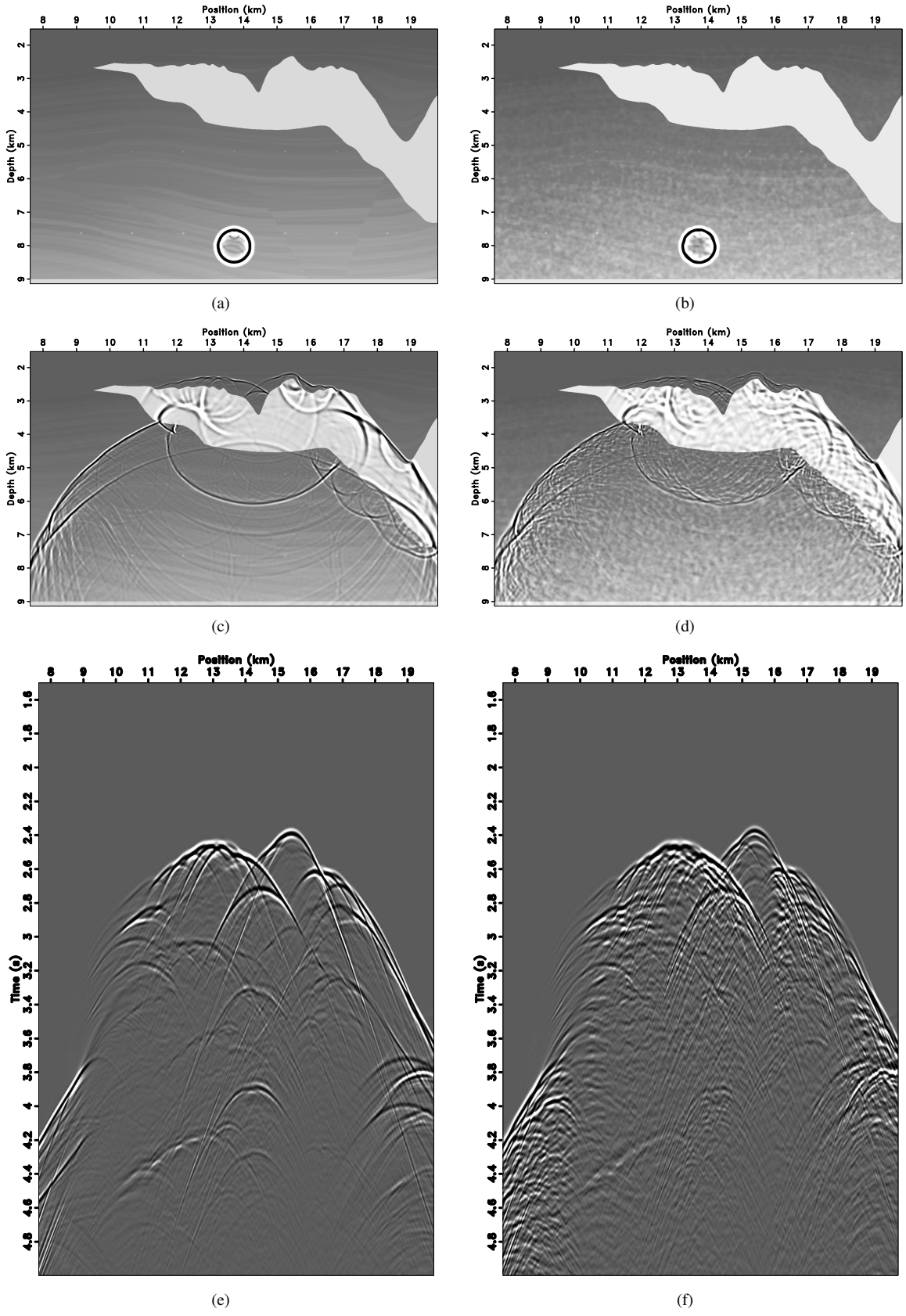


Figure 3. Seismic snapshots of acoustic wavefields simulated in the background velocity model (a)-(c), and in he random velocity model (b)-(d). Data recorded at the surface from simulation in the background velocity model (e) and from the simulation in the random velocity model (f).

simple transformations with efficient application to multi-dimensional signals. In this paper, we apply the pseudo WDF transformation to multi-dimensional seismic wavefields obtained by reconstruction from recorded seismic data. We use pseudo WDFs for decomposition and filtering of extrapolated space-time signals as a function of their local wavenumber-frequency. In particular, pseudo WDFs can filter reconstructed wavefields to retain their coherent components by removing high-frequency noise associated with random fluctuations in the wavefields due to random fluctuations in the model.

The idea for our method is simple: instead of imaging the reconstructed wavefields directly, we first filter them using pseudo WDFs to attenuate the random phase noise, and then proceed to imaging using a conventional or an extended imaging conditions. Wavefield filtering occurs during the application of the zero-frequency end-member of the pseudo WDF transformation, which reduces the random character of the field. For the rest of the paper, we use the abbreviation WDF to denote this special case of pseudo Wigner distribution functions, and not its general form.

As we described earlier, we can distinguish two options. The first option is to use wavefield parametrization as a function of data coordinates $\mathbf{x}$. In this case, we can write the pseudo WDF of the reconstructed wavefield $V(\mathbf{x},\mathbf{y},t)$ as

$$V_x(\mathbf{x},\mathbf{y},t) = \int_{|t_h|\leq T} dt_h \int_{|\mathbf{x}_h|\leq X} d\mathbf{x}_h \\ V\left(\mathbf{x}-\frac{\mathbf{x}_h}{2},\mathbf{y},t-\frac{t_h}{2}\right) V\left(\mathbf{x}+\frac{\mathbf{x}_h}{2},\mathbf{y},t+\frac{t_h}{2}\right) , \quad (4)$$

where $\mathbf{x}_h$ and t_h are variables spanning space and time intervals of total extent X and T, respectively. For 3D surface acquisition geometry, the 2D variable $\mathbf{x}_h$ is defined on the acquisition surface. The second option is to use wavefield parametrization as a function of image coordinates $\mathbf{y}$. In this case, we can write the pseudo WDF of the reconstructed wavefield $U(\mathbf{y},t)$ as

$$W_y(\mathbf{y},t) = \int_{|t_h|\leq T} dt_h \int_{|\mathbf{y}_h|\leq Y} d\mathbf{y}_h \\ U\left(\mathbf{y}-\frac{\mathbf{y}_h}{2},t-\frac{t_h}{2}\right) U\left(\mathbf{y}+\frac{\mathbf{y}_h}{2},t+\frac{t_h}{2}\right) , \quad (5)$$

where $\mathbf{y}_h$ and t_h are variables spanning space and time intervals of total extent Y and T, respectively. For 3D surface acquisition geometry, the 3D variable $\mathbf{y}_h$ is defined around image positions.

For the examples used in this section, we employ 41 grid points for the interval X centered around a particular receiver position, 5×5 grid points for the interval Y centered around a particular image point, and 21 grid points for the interval T centered around a particular time. These parameters are not necessarily optimal for the transformation, since they characterize the local WDF windows and depend on the specific implementation of the pseudo WDF transformation. The main criterion used for selecting the size of the space-time window for the pseudo WDF transformation is that of avoiding cross-talk between nearby events, e.g. reflections. Finding the optimal size of this window is an important consideration for our method, although its complete treatment falls outside the scope of the current paper and we leave it for future research. Preliminary results on optimal window selection are discussed by Borcea *et al.* (2006a).

Figure 4(b) depicts the results of applying the pseudo WDF transformation to the reconstructed wavefield in Figure 4(a). For the case of modeling in the random model and reconstruction in the background model, the pseudo WDF attenuates the random character of the wavefield significantly, Figure 4(b). The random character of the reconstructed wavefield is reduced and the main events cluster more closely around time $t=0$. Similarly, Figure 5(b) depicts the results of applying the pseudo WDF transformation to the reconstructed wavefields in Figure 5(a). For the case of modeling in the random model and reconstruction in the background model, the pseudo WDF also attenuates the random character of the wavefield significantly, Figure 5(b). The random character of the reconstructed wavefields is also reduced and the main events focus at the correct image location at time $t=0$.

2. 3 Zero-offset interferometric imaging condition

After filtering the reconstructed wavefields with pseudo WDFs, we can perform imaging with normal procedures. For the case of wavefields parametrized as a function of data coordinates, we obtain the total wavefield at image coordinates by summing over receiver coordinates $\mathbf{x}$

$$W_x(\mathbf{y},t) = \int_{\mathbf{x}} d\mathbf{x}\, V_x(\mathbf{x},\mathbf{y},t) , \quad (6)$$

followed by a conventional imaging condition extracting time $t=0$ from the pseudo WDF of the reconstructed wavefields:

$$R_x(\mathbf{y}) = W_x(\mathbf{y},t=0) . \quad (7)$$

The image obtained with this imaging procedure is shown in Figure 6(c). As expected, the artifacts caused by the unknown random fluctuations in the model are reduced, leaving a cleaner image of the source.

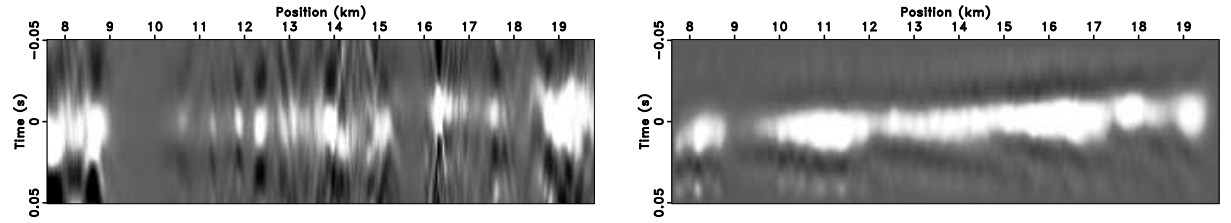
Similarly, for the case of wavefields parametrized as a function of image coordinates, we obtain the image by application of the conventional imaging condition extracting time $t=0$ from the pseudo WDF of the reconstructed wavefield:

$$R_y(\mathbf{y}) = W_y(\mathbf{y},t=0) . \quad (8)$$

The image obtained with this imaging procedure is shown in Figure 6(d). As in the preceding case, the artifacts caused by the unknown random fluctuations in the model are reduced, producing a cleaner image of the source, comparable with the one in Figure 6(c).

2. 4 Multi-offset interferometric imaging condition

The imaging procedure in equations 5-8 can be generalized for imaging prestack (multi-offset) data (Figure 1(b)). The con-



(a) (b)

Figure 4. Reconstructed seismic wavefield as a function of data coordinates (a) and its pseudo Wigner distribution function (b) computed as a function of data coordinates $\mathbf{x}$ and time t. The wavefield is reconstructed using the background model from data simulated in the random model.

ventional imaging procedure for this type of data consists of two steps (Claerbout, 1985): wavefield simulation from the source location to the image coordinates $\mathbf{y}$ and wavefield reconstruction at image coordinates $\mathbf{y}$ from data recorded at receiver coordinates $\mathbf{x}$, followed by an imaging condition evaluating the match between the simulated and reconstructed wavefields.

Let $U_S(\mathbf{y},t)$ be the source wavefield constructed from the location of the seismic source and $U_R(\mathbf{y},t)$ the receiver wavefield reconstructed from the receiver locations. A conventional imaging procedure produces a seismic image as the zero-lag of the time cross-correlation between the source and receiver wavefields. Mathematically, we can represent this operation as

$$R(\mathbf{y}) = \int_t dt\, U_S(\mathbf{y},t)\, U_R(\mathbf{y},t) \ , \tag{9}$$

where $R(\mathbf{y})$ represents the seismic image for a particular seismic experiment at coordinates $\mathbf{y}$. When multiple seismic experiments are processed, a complete image is obtained by summation of the images constructed for individual experiments. The actual reconstruction methods used to produce the wavefields $U_S(\mathbf{y},t)$ and $U_R(\mathbf{y},t)$ are irrelevant for the present discussion. As in the zero-offset/exploding reflector case, we use time-domain finite-difference solutions to the acoustic wave-equation, but any other reconstruction technique can be applied without changing the imaging approach.

When imaging in random media, the data recorded at the surface incorporates phase delays caused by the velocity variations encountered while waves propagate in the subsurface. In a typical seismic experiment, random phase delays accumulate both on the way from the source to the reflectors, as well as on the way from the reflectors to the receivers. Therefore, the receiver wavefield reconstructed using the background velocity model is characterized by random fluctuations, similar to the ones seen for wavefields reconstructed in the zero-offset situation. In contrast, the source wavefield is simulated in the background medium from a known source position and, therefore, it is not affected by random fluctuations. However, the zero-lag of the cross-correlations between the source wavefields (without random fluctuations) and the receiver wavefield (with random fluctuations), still generates image artifacts similar to the ones encountered in the zero-offset case.

Statistically stable imaging using pseudo WDFs can be obtained in this case, too. What we need to do is attenuate the phase errors in the reconstructed receiver wavefield and then apply a conventional imaging condition. Therefore, a multi-offset interferometric imaging condition can be formulated as

$$R(\mathbf{y}) = \int_t dt\, U_S(\mathbf{y},t)\, W_R(\mathbf{y},t) \ , \tag{10}$$

where $W_R(\mathbf{y},t)$ represents the pseudo WDF of the receiver wavefield $U_R(\mathbf{y},t)$ which can be constructed, in principle, either with parametrization relative to data coordinates, according to equations 4-6, or relative to image coordinates, according to equation 5. Of course, our choice is to use image-space parametrization for computational efficiency reasons.

2. 5 Discussion

The strategies described in the preceding section have notable similarities and differences. The imaging procedures 4-6-7 and 5-8 are similar in that they employ wavefields reconstructed from the surface data in similar ways. Neither method uses the surface recorded data directly, but they use wavefields reconstructed from those data as boundary conditions to numerical solutions of the acoustic wave-equation. The actual wavefield reconstruction procedure is identical in both cases.

The techniques are different because imaging with equations 4-6-7 employs independent wavefield reconstruction from receiver locations $\mathbf{x}$ to image locations $\mathbf{y}$. In practice, this requires separately solving the acoustic wave-equation, e.g. by time-domain finite-differences, from all receiver locations on the surface. Such computational effort is often prohibitive in practice. In contrast, imaging with equations 5-8 is similar to conventional imaging because it requires only one wavefield reconstruction using all recorded data at once, i.e. only one solution to the acoustic wave-equation, similar to conventional shot-record migration.

The techniques 4-6-7 and 5-8 are similar in that they both employ noise suppression using pseudo Wigner distribution functions. However, the methods are parametrized differently, the former relative to data coordinates with 2D local space averaging and the later relative to image coordinates with 3D local space averaging.

The imaging functionals presented in this paper are described as functions of space coordinates, $\mathbf{x}$ or $\mathbf{y}$, and time,

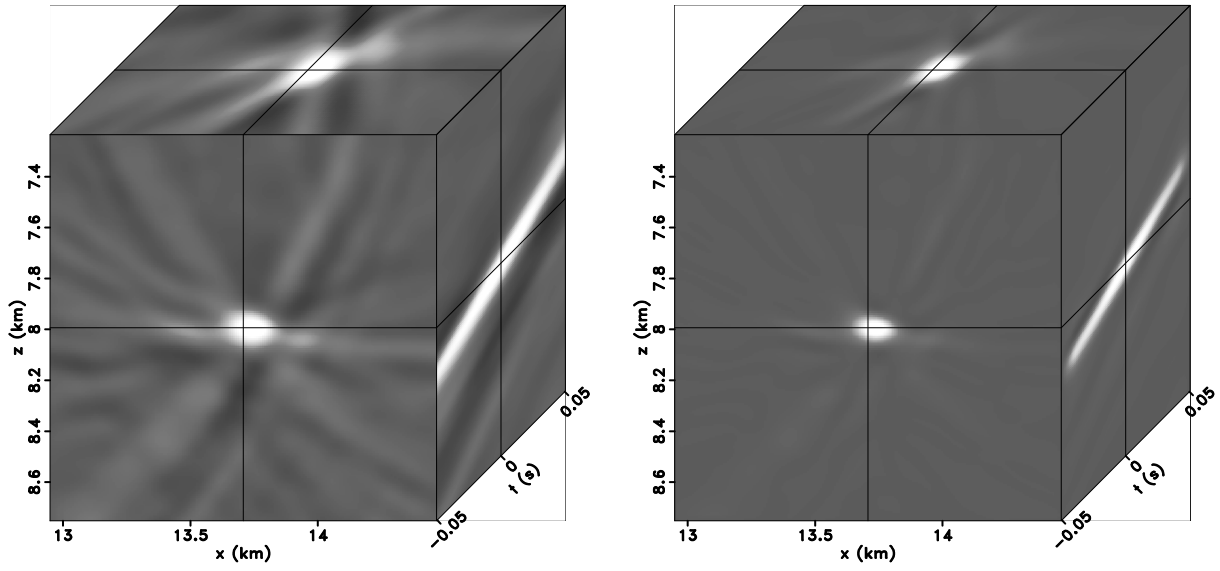


Figure 5. Reconstructed seismic wavefield as a function of image coordinates (a) and its pseudo Wigner distribution function (b) computed as a function of image coordinates $\mathbf{y}$ and time t.The wavefield is reconstructed using the background model from data modeled in the random model.

t. As suggested in Appendix C, pseudo WDFs can be implemented either in time or frequency, so potentially the imaging conditions discussed in this paper can also be implemented in the frequency-domain. However, we restrict our attention in this paper to the time-domain implementation and leave the frequency-domain implementation subject to future study.

Equations 4-6-7 can be collected into the zero-offset imaging functional

$$R_{CINT}\left(\mathbf{y}\right) = \int_t dt\ \delta\left(t\right) \int_{\mathbf{x}} d\mathbf{x} \int_{|t_h|\leq T} dt_h \int_{|\mathbf{x}_h|\leq X} d\mathbf{x}_h$$
$$V\left(\mathbf{x}-\frac{\mathbf{x}_h}{2},\mathbf{y},t-\frac{t_h}{2}\right) V\left(\mathbf{x}+\frac{\mathbf{x}_h}{2},\mathbf{y},t+\frac{t_h}{2}\right)\ , \quad (11)$$

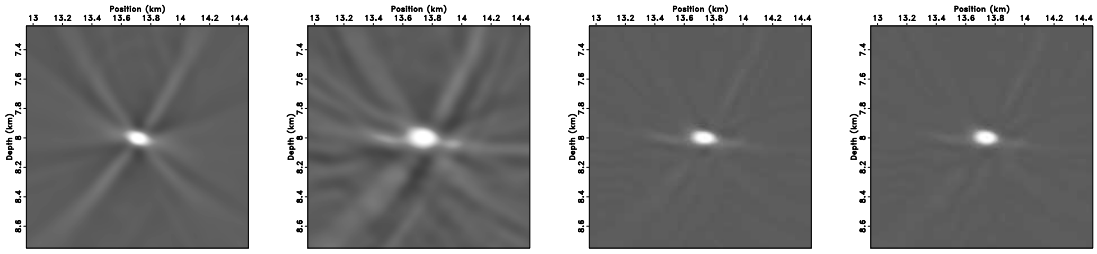
where the temporal δ function implements the zero time imaging condition. A similar form can be written for the multi-offset case. Equation 11 corresponds to the time-domain version of the coherent interferometric functional proposed by Borcea *et al.* (2006a,b,c). Consistent with the preceding discussion, the cost required to implement this imaging functional is often prohibitive for practical application to seismic imaging problems.

3 STATISTICAL STABILITY

The interferometric imaging condition described in the preceding section is used to reduce imaging artifacts by attenuating the incoherent energy corresponding to velocity errors, as illustrated in Figures 6(b) and 6(d). The random model used for this example corresponds to the weak fluctuation regime, as explained in Appendix A (characteristic wavelength of similar scale with the random fluctuations in the medium and fluctuations with small magnitude).

By statistical instability we mean that images obtained for different realizations of random models with the identical statistics are different. Figures 7(a)-7(c) illustrate data modeled for different realizations of the random model in Figure 3(b). The general kinematics of the data are the same, but subtle differences exist between the various datasets due to the random model variations. Migration using a conventional imaging condition leads to the images in Figures 7(d)-7(f) which also show variations from one realization to another. In contrast, Figures 7(g)-7(i) show images obtained by the interferometric imaging condition in equations 5-8, which are more similar to one-another since many of the artifacts have been attenuated.

In typical seismic imaging problems, we cannot ensure that random velocity fluctuations are small (e.g. $\sigma \leq 5\%$). It is desirable that imaging remains statistically stable even in cases when velocity varies with larger magnitude. We investigate the statistical properties of the imaging functional in equations 5-8 using numerical experiments similar to the one used earlier. We describe the random noise present in the velocity models using the following parameters explained in Appendix A: seismic spatial wavelength $\lambda = 76.2$ m, wavelet central frequency $\omega = 20$ Hz, random fluctuations parameters: $r_a = 0.0762$, $r_c = 0.0762$, $\alpha = 2$, and random noise magnitude σ between 15% and 45%. This numerical experiment simulates a situation that mixes the theoretical regimes explained in Appendix B: random model fluctuations of comparable scale with the seismic wavelength lead to destruction of the wavefronts, as suggested by the "weak fluctuations" regime; large magnitude of the random noise leads to diffusion of the wavefronts,



(a) (b) (c) (d)

Figure 6. Images produced by the conventional imaging condition using the data simulated in the background model (a) and using the data simulated in the random model (b). Images produced from data simulated in the random model using the interferometric imaging condition with parametrization as a function of data coordinates (c) and as a function of image coordinates (d).

as suggested by the "diffusion approximation" regime. This combination of parameters could be regarded as a worst-case-scenario from a theoretical standpoint.

Figures 8(a)-8(c) show data simulated in models similar to the one depicted in Figure 3(b), but where the random noise component is described by $\sigma = 15, 30, 45\%$, respectively. As expected, the wavefronts recorded at the surface are increasingly distorted to the point where some of the later arrival are not even visible in the data.

Migration using a conventional imaging condition leads to the images in Figures 8(d)-8(f). As expected, the images show stronger artifacts due to the larger defocusing caused by the unknown random fluctuations in the model. However, migration using the interferometric imaging condition leads to the images in Figures 8(g)-8(i). Artifacts are significantly reduced and the images are much better focused.

4 MULTI-OFFSET IMAGING EXAMPLES

There are many potential applications for this interferometric imaging functional. One application we illustrate in this paper is imaging of complex stratigraphy through a medium characterized by unknown random variations. In this situation, accurate imaging using conventional methods requires velocity models that incorporate the small scale (random, as we view them) velocity variations. However, practical migration velocity analysis does not produce models of this level of accuracy, but approximates them with smooth, large-scale fluctuations one order of magnitude larger than that of the typical seismic wavelength. Here, we study the impact of the unknown (random) component of the velocity model on the images and whether interferometric imaging increases the statistical stability of the image.

For all our examples, we extrapolate wavefields using time-domain finite-differences both for modeling and for migration. Thus, we simulate a reverse-time imaging procedure, although the theoretical results derived in this paper apply equally well to other wavefield reconstruction techniques, e.g. downward continuation, Kirchhoff integral methods, etc. The parameters used in our examples, explained in Appendix A, are: seismic spatial wavelength $\lambda = 76.2$ m, wavelet central frequency $\omega = 20$ Hz, random fluctuations parameters: $r_a = 76.2$ m, $r_c = 76.2$ m, $\alpha = 2$, and random noise magnitude $\sigma = 20\%$.

Consider the model depicted in Figures 10(a)-10(d). As in the preceding example, the left panels depict the known smooth velocity v_0, and the right panels depict the model with random variations. The imaging target is represented by the oblique lines, Figure 9(b), located around $z = 8$ km, which simulates a cross-section of a stratigraphic model.

We model data with a random velocity model and image using the smooth model. Figures 10(a)-10(d) show wavefield snapshots in the two models for different propagation times, one before the source wavefields interact with the target reflectors and one after this interaction. The propagating waves are affected the the random fluctuations in the model both before and after their interaction with the reflectors. Figures 10(e) and 10(f) show the corresponding recorded data on the acquisition surface located at $z = \lambda$, where λ represents the wavelength of the source pulse.

Migration with a conventional imaging condition of the data simulated in the background model using the same velocity produces the image in Figure 11(a). The targets are well imaged, although the image also shows artifacts due to truncation of the data on the acquisition surface. In contrast, migration with the conventional imaging condition of the data simulated in the random model using the background velocity produces the image in Figure 11(b). This image is distorted by the random variations in the model that are not accounted for in the background migration velocity. The targets are harder to discern since they overlap with many truncation and defocusing artifacts caused by the inaccurate migration velocity.

Finally, Figure 11(c) shows the migrated image using the interferometric imaging condition applied to the wavefields reconstructed in the background model from the data simulated in the random model. Many of the artifacts caused by the inaccurate velocity model are suppressed and the imaging targets are more clearly visible and easier to interpret. Furthermore, the general patterns of amplitude variation along the imaged reflectors are similar between Figures 11(b) and 11(c).

We note that the reflectors are not as well imaged as the ones obtained when the velocity is perfectly known. This is because the interferometric imaging condition described in this

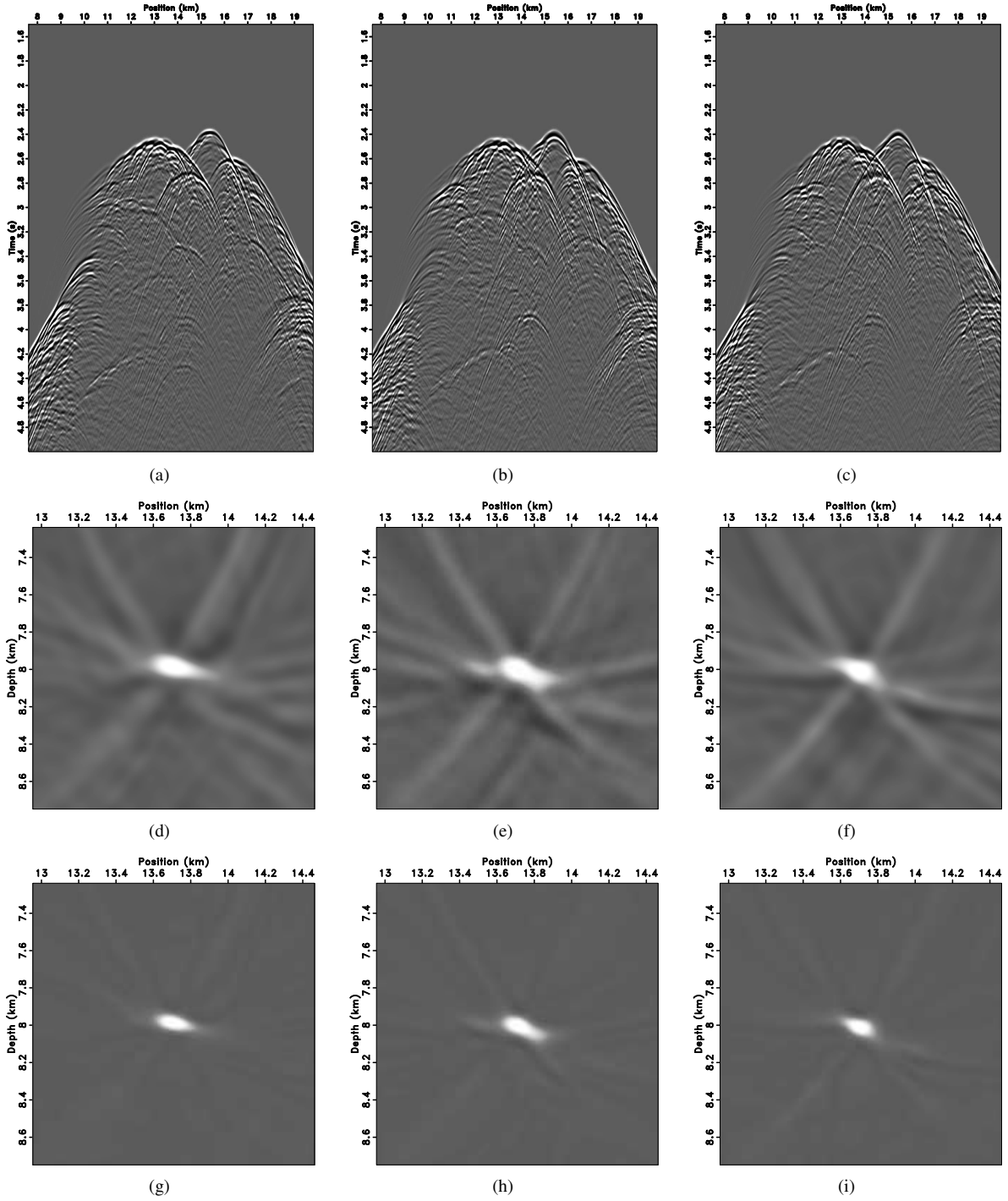


Figure 7. Illustration of statistical stability for the interferometric imaging condition in presence of random model variations. Data modeled using velocity with random variations of magnitude $\sigma = 30\%$, for different realizations of the noise model n. Images obtained by conventional imaging (d)-(f) and images obtained by interferometric imaging (g)-(i).

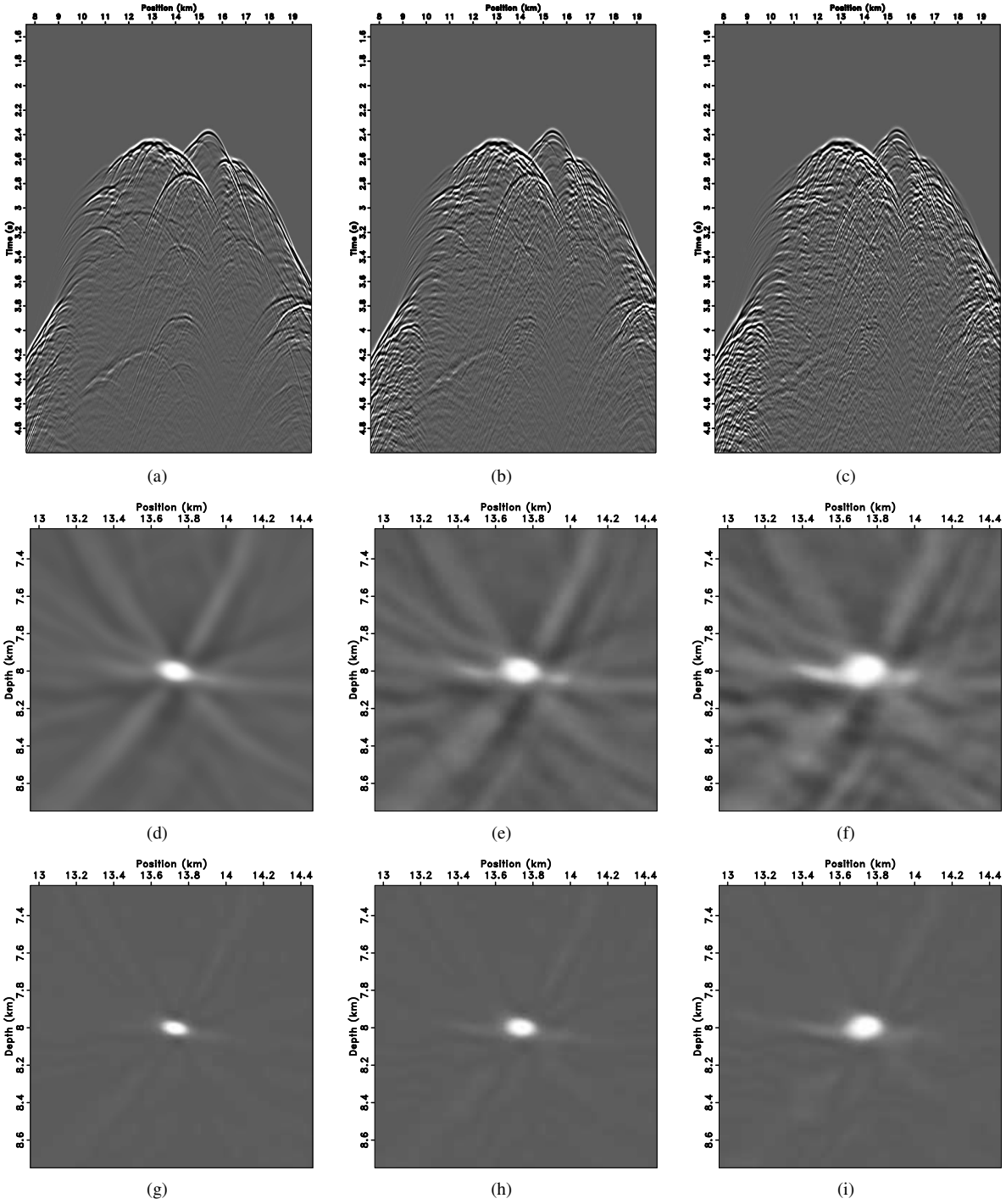


Figure 8. Illustration of interferometric imaging condition robustness in presence of random model variations. Data modeled using velocity with random variations of magnitudes $\sigma = 15\%$ (a), $\sigma = 30\%$ (b), and $\sigma = 45\%$ (c). Images obtained by conventional imaging (d)-(f) and images obtained by interferometric imaging (g)-(i).

paper does not correct kinematic errors due to inaccurate velocity. It only acts on the extrapolated wavefields to reduce wavefield incoherency and add statistical stability to the imaging process. Further extensions to the interferometric imaging condition can improve focusing and enhance the images by correcting wavefields prior to imaging. However, this topic falls outside the scope of this paper and we do not elaborate on it further.

5 CONCLUSIONS

We extend the conventional seismic imaging condition based on wavefield cross-correlations to achieve statistical stability for models with rapid, small-scale velocity variation. We assume that the random velocity variations on a scale comparable with the seismic wavelength are modeled by correlated Gaussian distributions. Our proposed interferometric imaging condition achieves statistical stability by applying conventional imaging to the Wigner distribution functions of the reconstructed seismic wavefields. The interferometric imaging condition is a natural extension of the cross-correlation imaging condition and adds minimally to the cost of migration. The main characteristic of the method is that it operates on extrapolated wavefields at image positions (thus the name interferometric imaging condition), in contrast with costlier alternative approaches using interferometry parametrized as a function of receiver coordinates.

6 ACKNOWLEDGMENTS

We acknowledge Geophysics Associate Editor John Etgen for numerous comments and suggestions which have significantly improved the manuscript. This work is partially supported by the sponsors of the Consortium Project at the Center for Wave Phenomena at Colorado School of Mines.

REFERENCES

Baysal, E., Kosloff, D. D., and Sherwood, J. W. C., 1983, Reverse time migration: Geophysics, **48**, no. 11, 1514–1524.

Borcea, L., Papanicolaou, G., and Tsogka, C., 2006a, Adaptive interferometric imaging in clutter and optimal illumination: Inverse Problems, **22**, 1405–1436.

——— 2006b, Coherent interferometric imaging in clutter: Geopysics, **71**, no. 4, SI165–SI175.

——— 2006c, Coherent interferometry in finely layered random media: SIAM Journal on Multiscale Modeling and Simulation, **5**, no. 1, 62–83.

Claerbout, J. F., 1985, Imaging the Earth's interior: , Blackwell Scientific Publications.

Cohen, L., 1995, Time Frequency Analysis: , Prentice Hall Signal Processing Series.

Fink, M., 1999, Time-reversed acoustics: Scientific American, **281**, 91–97.

Fouque, J., Garnier, J., Nachbin, A., and Solna, K., 2005, Time reversal refocusing for point source in randomly layered media: Wave Motion, **42**, 191–288.

Loewenthal, D., Lu, L., Roberson, R., and Sherwood, J., 1976, The wave equation applied to migration: Geophys. Prosp., **24**, no. 02, 380–399.

Papanicolaou, G., Ryzhik, L., and Solna, K., 2004, Statistical stability in time reversal: SIAM J. Appl. Math., **64**, 1133–1155.

Pratt, R. G., and Worthington, M. H., 1990, Inverse theory applied to multi-source cross-hole tomography. part 1: Acoustic wave-equation method: Geophys. Prosp., **38**, no. 03, 287–310.

Pratt, R. G., 1990, Inverse theory applied to multi-source cross-hole tomography. part 2: Elastic wave-equation method: Geophys. Prosp., **38**, no. 03, 311–312.

Sava, P., and Biondi, B., 2004a, Wave-equation migration velocity analysis - I: Theory: Geophysical Prospecting, **52**, 593–606.

——— 2004b, Wave-equation migration velocity analysis - II: Subsalt imaging examples: Geophysical Prospecting, **52**, 607–623.

Shen, P., Symes, W., Morton, S., and Calandra, H., 2005, Differential semblance velocity analysis via shot profile migration: 74th Annual International Meeting, SEG, Expanded Abstracts, 2249–2253.

Sirgue, L., and Pratt, R., 2004, Efficient waveform inversion and imaging: A strategy for selecting temporal frequencies: Geophysics, **69**, no. 1, 231–248.

Tarantola, A., 1987, Inverse Problem Theory: methods for data fitting and model parameter estimation: , Elsevier.

Ville, J., 1948, Theorie et applications de la notion de signal analytique: Cables et Transmissions, **2A**, 61–74.

Wigner, E., 1932, On the quantum correction for thermodynamic equilibrium: Physical Review, **40**, 749–759.

Woodward, M. J., 1992, Wave-equation tomography: Geophysics, **57**, no. 01, 15–26.

7 APPENDIX A: NOISE MODEL

Consider a medium whose behavior is completely defined by the acoustic velocity, i.e. assume that the density $\rho\left(x,y,z\right)=\rho_0$ is constant and the velocity $v\left(x,y,z\right)$ fluctuates around a homogenized value $v_0\left(x,y,z\right)$ according to the relation

$$\frac{1}{v^2\left(x,y,z\right)}=\frac{1+\sigma m\left(x,y,z\right)}{v_0^2\left(x,y,z\right)}\;, \tag{A-1}$$

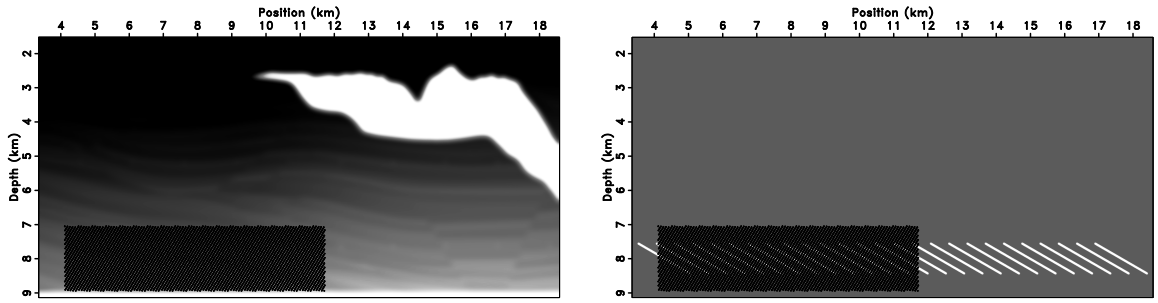
where the parameter m characterizes the type of random fluctuations present in the velocity model, and σ denotes their strength.

Consider the covariance orientation vectors

$$\mathbf{a} = \left(a_x,a_y,a_z\right)^\top\in\mathbb{R}^3 \tag{A-2}$$

$$\mathbf{b} = \left(b_x,b_y,b_z\right)^\top\in\mathbb{R}^3 \tag{A-3}$$

$$\mathbf{c} = \left(c_x,c_y,c_z\right)^\top\in\mathbb{R}^3 \tag{A-4}$$



(a) (b)

Figure 9. Velocity model (a) and imaging target located around $z = 8$ km (b). The model consists of a smooth version of the Sigsbee2A velocity, in order to avoid backscattering during reverse-time migration. The shaded area is imaged in Figures 11(a)-11(c).

defining a coordinate system of arbitrary orientation in space. Let $r_a, r_b, r_c > 0$ be the covariance range parameters in the directions of $\mathbf{a}$,$\mathbf{b}$ and $\mathbf{c}$, respectively.

We define a covariance function

$$\mathrm{cov}\,(x,y,z) = \exp\left[-l^{\alpha}\,(x,y,z)\right]\ , \tag{A-5}$$

where $\alpha \in [0,2]$ is a distribution shape parameter and

$$l\,(x,y,z) = \sqrt{\left(\frac{\mathbf{a}\cdot\mathbf{r}}{r_a}\right)^2 + \left(\frac{\mathbf{b}\cdot\mathbf{r}}{r_b}\right)^2 + \left(\frac{\mathbf{c}\cdot\mathbf{r}}{r_c}\right)^2} \tag{A-6}$$

is the distance from a point at coordinates $\mathbf{r} = (x,y,z)$ to the origin in the coordinate system defined by $\{r_a\mathbf{a}, r_b\mathbf{b}, r_c\mathbf{c}\}$.

Given the IID Gaussian noise field $n\,(x,y,z)$, we obtain the random noise $m\,(x,y,z)$ according to the relation

$$m\,(x,y,z) = F^{-1}\left[\sqrt{\widehat{\mathrm{cov}}\,(k_x,k_y,k_z)}\;\widehat{n}\,(k_x,k_y,k_z)\right]\ , \tag{A-7}$$

where k_x, k_y, k_z are wavenumbers associated with the spatial coordinates x, y, z, respectively. Here,

$$\widehat{\mathrm{cov}} \;=\; F\left[\mathrm{cov}\right] \tag{A-8}$$

$$\widehat{n} \;=\; F\left[n\right] \tag{A-9}$$

are Fourier transforms of the covariance function cov and the noise n, $F[\cdot]$ denotes Fourier transform, and $F^{-1}[\cdot]$ denotes inverse Fourier transform. The parameter α controls the visual pattern of the field, and $\mathbf{a}, \mathbf{b}, \mathbf{c}, r_a, r_b, r_c$ control the size and orientation of a typical random inhomogeneity.

8 APPENDIX B: WAVE PROPAGATION AND SCALE REGIMES

Acoustic waves characterized by pressure $p\,(x,y,z,t)$ propagate according to the second order acoustic wave-equation for constant density

$$\frac{\partial^2 p}{\partial t^2} = v^2\nabla^2 p + F_\lambda(t)\ , \tag{B-1}$$

where $F_\lambda\,(t)$ is a wavelet of characteristic wavelength λ.

Given the parameters l (size of inhomogeneities), λ (wavelength size), L (propagation distance) and σ (noise strength), we can define several propagation regimes.

The *weak fluctuations regime* characterized by waves with wavelength of size comparable to that of typical inhomogeneities propagating over a medium with small fluctuations to a distance of many wavelengths. This regime is characterized by negligible back scattering, and the randomness impacts the propagating waves through forward multipathing. The relevant length parameters are related by

$$l \sim \lambda \ll L\ , \tag{B-2}$$

and the noise strength is assumed small

$$\sigma \ll 1\ . \tag{B-3}$$

The *diffusion approximation regime* characterized by waves with wavelength much larger than that of typical inhomogeneities propagate over a medium with strong fluctuations to a distance of many wavelengths. This regime is characterized by traveling waves that are statistically stable but diffuse with time. Back propagation of such waves in a medium without random fluctuations results in loss of resolution. The relevant length parameters are related by

$$l \ll \lambda \ll L\ , \tag{B-4}$$

and the noise strength is not assumed small

$$\sigma \sim 1\ . \tag{B-5}$$

9 APPENDIX C: WIGNER DISTRIBUTION FUNCTIONS

Consider the complex signal $u\,(t)$ which depends on time t. By definition, its *Wigner distribution function* (WDF) is (Wigner, 1932):

$$W\,(t,\omega) = \frac{1}{2\pi}\int u^*\left(t-\frac{t_h}{2}\right)u\left(t+\frac{t_h}{2}\right)e^{-i\,\omega\,t_h}dt_h\ , \tag{C-1}$$

where ω denotes temporal frequency, t_h denotes the relative time shift of the considered signal relative to a reference time t and the sign * denotes complex conjugation of complex signal

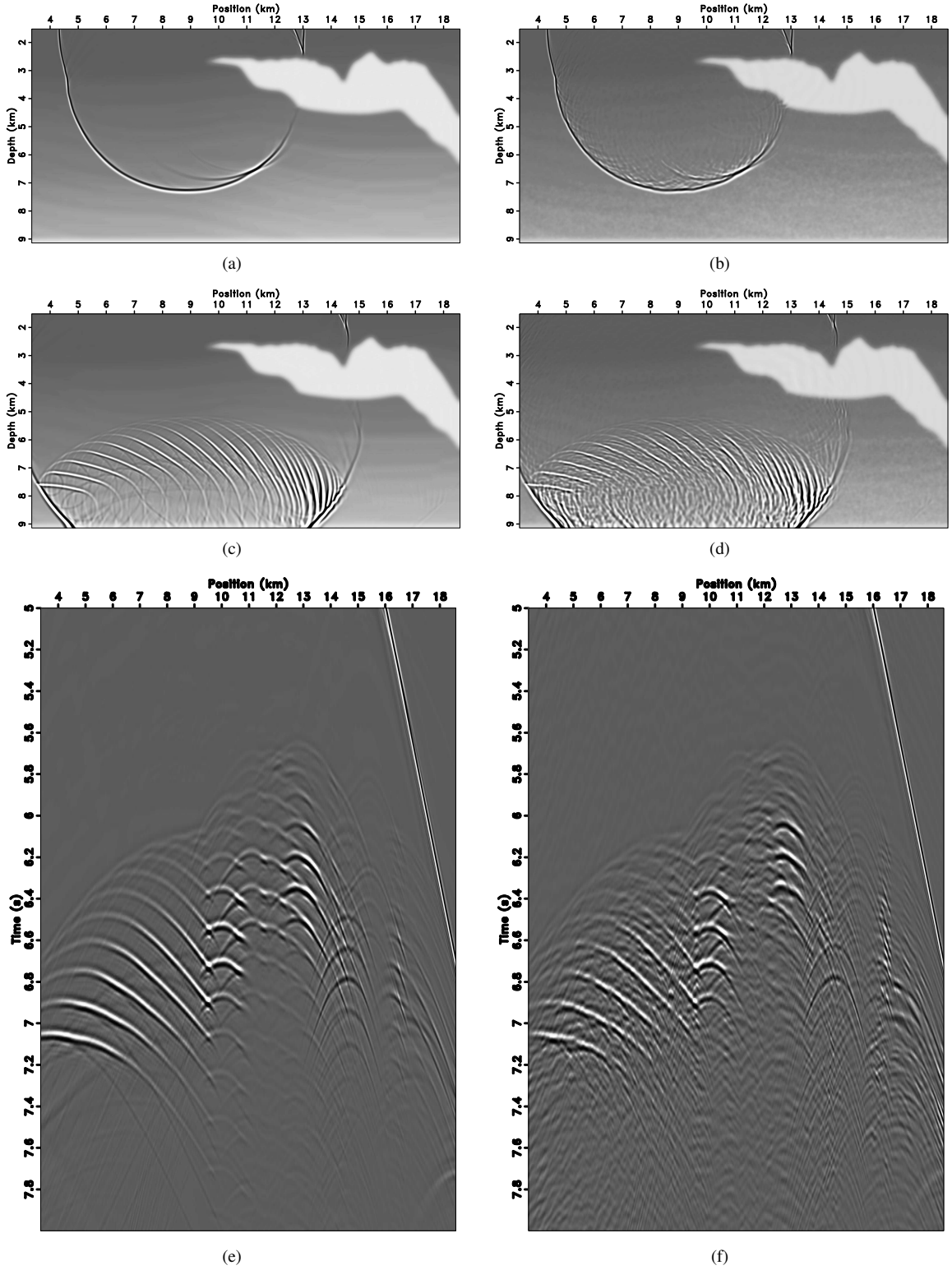


Figure 10. Seismic snapshots of acoustic wavefields simulated in the background velocity model (a)-(c), and in the random velocity model (b)-(d). Data recorded at the surface from the simulation in the background velocity model (e) and from the simulation in the random velocity model (f).

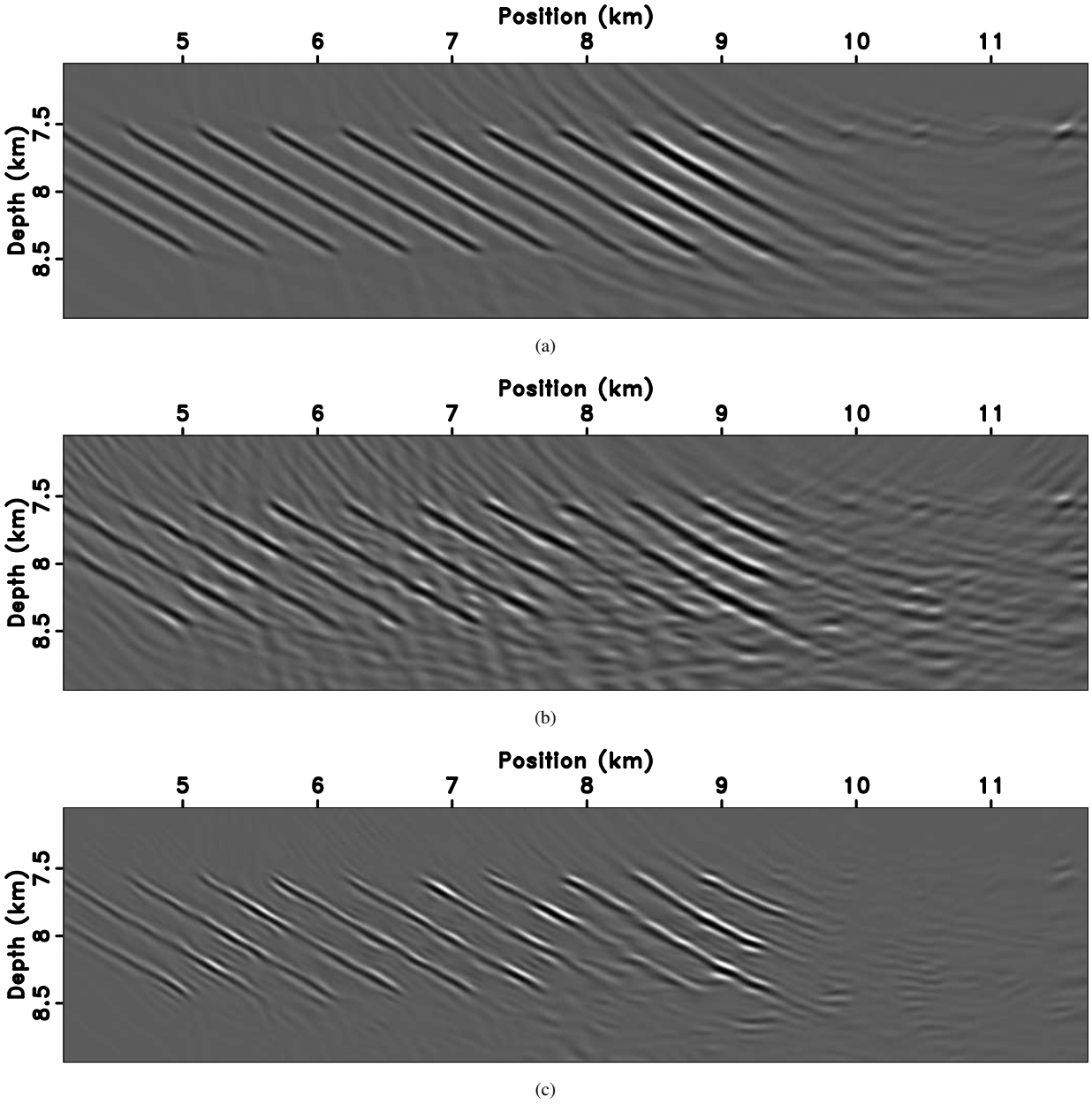


Figure 11. Image produced using the conventional imaging condition from data simulated in the background model (a) and from data simulated in the random model (b). Image produced using the interferometric imaging condition from data simulated in the random model (c).

s. The same WDF can be obtained in terms of the spectrum $U(\omega)$ of the signal $u(t)$:

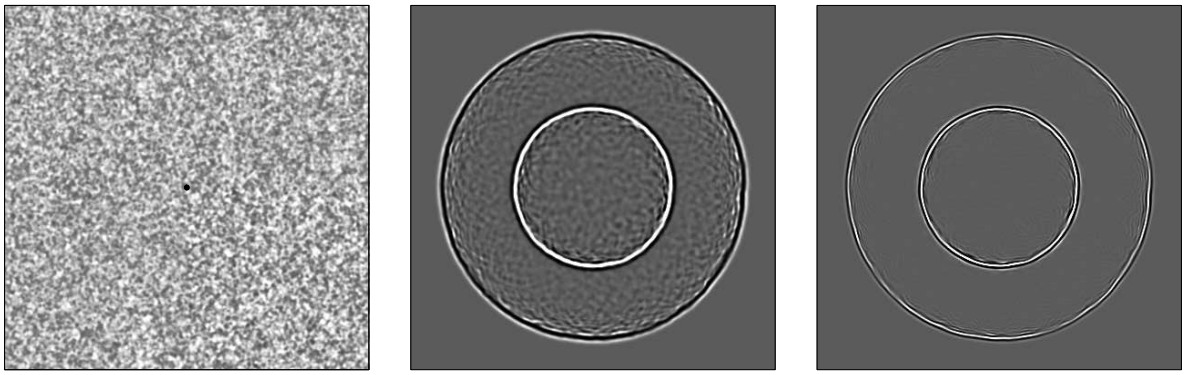
$$W(t,\omega) = \frac{1}{2\pi}\int U^*\left(\omega + \frac{\omega_h}{2}\right) U\left(\omega - \frac{\omega_h}{2}\right) e^{-i\,t\,\omega_h} d\omega_h \ , \tag{C-2}$$

where ω_h denotes the relative frequency shift of the considered spectrum relative to a reference frequency ω. The time integral in equation C-1 or the frequency integral in equation C-2 spans the entire domain of time and frequency, respectively. When the interval is limited to a region around the reference value, the transformation is known as *pseudo Wigner distribution function*.

A special subset of the transformation equation C-1 corresponds to zero temporal frequency. For input signal $u(t)$, we obtain the output Wigner distribution function $W(t)$ as

$$W(t) = \frac{1}{2\pi}\int u^*\left(t - \frac{t_h}{2}\right) u\left(t + \frac{t_h}{2}\right) dt_h \ . \tag{C-3}$$

The WDF transformation can be generalized to multi-dimensional signals of space and time. For example, for 2D



(a) (b) (c)

Figure C-1. Random velocity model (a), wavefield snapshot simulated in this model by acoustic finite-differences (b), and its 2D pseudo Wigner distribution function (c).

real signals function of space, $u\,(x,y)$, the zero-wavenumber pseudo WDF can be formulated as

$$W\,(x,y) = \frac{1}{4\pi^2} \int\limits_{|x_h|\leq X} \int\limits_{|y_h|\leq Y} u\left(x-\frac{x_h}{2}, y-\frac{y_h}{2}\right) \times u\left(x+\frac{x_h}{2}, y+\frac{y_h}{2}\right) dx_h dy_h \;, \quad \text{(C-4)}$$

where x_h and y_h denote relative shift of the signal s relative to positions x and y, respectively. In this particular form, the pseudo WDF transformation has the property that it filters the input of random fluctuations preserving in the output image the spatially coherent components in a noise-free background.

For illustration, consider the model depicted in Figure 1(a). This model consists of a smoothly-varying background with 25% random fluctuations. The acoustic seismic wavefield corresponding to a source located in the middle of the model is depicted in Figure 1(b). This wavefield snapshot can be considered as the random "image". The application of the 2D pseudo WDF transformation to images shown in Figure 1(b) produces the image shown in Figure 1(c). We can make three observations on this image: first, the random noise is strongly attenuated; second, the output wavelet is different from the input wavelet, as a result of the bi-linear nature of the pseudo WDF transformations; third, the transformation is isotropic, i.e. it operates identically in all directions. The pseudo WDF applied to this image uses 11×11 grid points in the vertical and horizontal directions. As indicated in the body of the paper, we do not discuss here the optimal selection of the WDF window. Further details of Wigner distribution functions and related transformations are discussed by Cohen (1995).